RSC Advances

PAPER

View Article Online
View Journal | View Issue

Cite this: *RSC Adv.*, 2025, **15**, 18518

Design, fabrication and characterization of a magnetite-chitosan coated iron-based metal–organic framework (Fe_3O_4@chitosan/MIL-100(Fe)) for efficient curcumin delivery as a magnetic nanocarrier†

Fatemeh Parsa,[a] Moslem Setoodehkhah *[a] and Seyed Mohammad Atyabi [b]

Curcumin, a natural polyphenol with potent anticancer and anti-inflammatory properties, has significant limitations in biomedical applications due to its poor water solubility, rapid metabolism, and low bioavailability. To overcome these challenges, drug delivery systems such as metal–organic frameworks (MOFs) have been explored. This study developed a magnetic nanocomposite, Fe_3O_4@chitosan/MIL-100(Fe), designed to enhance curcumin delivery. The nanocomposite consists of a magnetic Fe_3O_4 core coated with biocompatible chitosan, which facilitates MOF (MIL-100(Fe)) growth, improving drug-loading capacity and targeted delivery potential. Different ratios of magnetite-coated chitosan to MOF were evaluated, with the optimal 1 : 1 ratio achieving an exceptional drug loading efficiency (DLE) of 95.36% within 24 hours and a drug loading content (DLC) of 48.81%. Brunauer–Emmett–Teller (BET) and EDX-mapping analyses confirmed that curcumin was effectively encapsulated within the nanocomposite's porous structure and uniformly adsorbed on its surface. Adsorption studies indicated that curcumin adsorption followed the Freundlich isotherm model, while kinetic analysis showed strong agreement with the intraparticle diffusion and Korsmeyer–Peppas models. Notably, the curcumin-loaded Fe_3O_4@CS/MIL-100(Fe) demonstrated greater cytotoxicity against breast cancer cells (MCF-7) than free curcumin and the unloaded nanocarrier while exhibiting lower toxicity toward normal human dermal fibroblast (HDF) cells, as confirmed by MTT assays. These findings suggest that Fe_3O_4@CS/MIL-100(Fe) offers a promising strategy to overcome curcumin's inherent limitations, paving the way for more effective targeted drug delivery systems.

Received 7th January 2025
Accepted 28th May 2025

DOI: 10.1039/d5ra00162e

rsc.li/rsc-advances

1 Introduction

Advancements in drug delivery systems have revolutionized the precision and control of drug release within specific target areas, utilizing strategies such as erodible materials, degradable matrices, hydrogels, osmotic pumps, and reservoirs to ensure efficient delivery to tissues, cells, or organs. Despite these innovations, challenges such as distribution, solubility, drug aggregation, target selection, and treatment efficacy remain significant obstacles. These systems play a critical role in complementing drug development, which focuses on discovering and creating new medications through research, synthesis, and rigorous testing.[1] The drug development process is inherently complex and costly, with approximately 40% of research efforts failing due to unpredictable biological responses and human toxicity.[2,3] To address these challenges, nanotechnology has emerged as a transformative tool in both drug development and delivery, offering nanoscale carriers that enhance treatment outcomes and improve life expectancy.[4] Inspired by Paul Ehrlich's concept of 'magic bullets,' scientific efforts are now directed toward designing nanoscale drug delivery systems capable of precise targeting and controlled release.[5] Importantly, drug delivery systems undergo a stepwise evaluation process, beginning with laboratory-based preclinical testing to assess safety and efficacy. Only when these results prove satisfactory are *in vivo* tests conducted within the body, further validating the system's performance and therapeutic potential. Together, these advancements in drug development and delivery strive to overcome existing limitations, refine treatment strategies, and optimize patient outcomes.

In this context, the development of biocompatible and targeted drug delivery systems is crucial to reducing off-target toxicity and improving therapeutic efficacy. The Fe_3O_4@chitosan/MIL-100(Fe) nanocomposite developed in this study

[a]*Department of Inorganic Chemistry, Faculty of Chemistry, University of Kashan, Kashan, Iran. E-mail: setoodehkhah@kashanu.ac.ir*

[b]*PhD Department of Pilot Biotechnology Pasteur Institute of Iran Tehran, Iran*

† Electronic supplementary information (ESI) available. See DOI: https://doi.org/10.1039/d5ra00162e

integrates a biocompatible chitosan coating with a magnetite-MOF hybrid structure, aiming to enhance drug stability, bioavailability, and selective delivery while minimizing adverse host responses.

Among the promising candidates, metal–organic frameworks (MOFs) stand out. MOFs offer a high surface area, drug incorporation capabilities, and versatility in synthesis. However, achieving a delicate balance between stability and degradation, controlling surface modifications, and addressing challenges related to MOF chemical stability remain critical considerations for effective utilization in biomedical applications.[6,7]

Iron-based Metal–Organic Frameworks (Fe-MOFs) have gained prominence in drug delivery and bioimaging due to their unique properties. However, to enable widespread use, overcoming challenges such as high energy consumption and environmentally hazardous synthesis methods is crucial for scaling up production.[8] Among Fe-MOFs, MIL-100(Fe) and MIL-101(Fe) exhibit stability in biological fluids. Their high tunability, porosity, and ease of functionalization make them promising candidates for targeted drug delivery systems.[9] Additionally, the MIL family of mainly iron carboxylates represents biodegradable candidates for drug delivery, combining a minimally toxic metal with a highly polar ligand that can be easily removed from the body.[7] For instance, Fe-MIL-100, when used as an inhalable carrier for theophylline, exhibits minimal impact on cell viability even at high concentrations.[10]

Iron oxides, specifically magnetite nanoparticles (Fe_3O_4-NPs), are widely employed due to their unique properties. Magnetite (Fe_3O_4) adopts an inverse spinel pattern in its crystal structure[11] and possesses exceptional magnetic strength, making it the strongest magnetic mineral on Earth. These Fe_3O_4-NPs exhibit biocompatibility, biodegradability, and low toxicity to humans, positioning them as promising materials for future biomedical applications.[12–14] The synergistic effects of magnetic separation and high porosity hold promise for developing efficient drug delivery systems.[15] In a study by Gumma *et al.*, Fe_3O_4@MIL-100(Fe) was synthesized *via* an *in situ* hydrothermal route at 150 °C for 12 hours, using HF and HNO_3 as agents for the anticancer drug doxorubicin hydrochloride (DOX).[16]

To address the aggregation tendency of magnetite and MIL particles[17,18] and enhance surface interactions, researchers have introduced a hydrophilic interlayer.[19] Fei Ke and colleagues designed a core–shell structure using (methacrylic acid, MAA)-functionalized Fe_3O_4 nanoparticles as an Ibuprofen adsorbent.[20] Additionally, silica layers have been employed in other studies to modify the surface of magnetite particles.[15,19,21] Chitosan, known for its pH-responsive properties in drug delivery systems, contains numerous hydrophilic groups making it an effectively modify the surface of Fe_3O_4. Chitosan-coated metal–organic frameworks (MOFs) can demonstrated the ability to retain their structure and porosity while enhancing stability in physiological fluids.[22] Horcajada and colleagues demonstrate that chitosan coating on the external surface of MIL-100(Fe) preserved the crystalline structure and high porosity of the MOF. They estimated the positive impact of coated chitosan on chemical stability through fluorescence studies of impregnated nanoparticles functionalized with rhodamine-labeled chitosan under simulated oral conditions.[23] Given its unique combination of bioadhesive properties, biocompatibility, biodegradability, low immunogenicity, efflux pump inhibition, and high cellular permeability, chitosan is as an ideal material for local drug delivery applications.[24–26] Researchers have developed chitosan-coated nanoparticles for the encapsulate and targeted transport active compounds, enabling targeted delivery to specific tissues or cells.[27] For instance, Hassan Namazi and co-workers designed CS/Zn-MOF@GO microspheres as a pH-responsive carrier for 5-fluorouracil, reporting twice the release at pH 5.0 compared to pH 7.4.[28] The Warburg effect in cancer cells leads to excessive lactic acid production and consequently lowers the pH in tumor microenvironments. Chitosan (CS) absorbs water and swells under acidic conditions, resulting in a more porous polymer structure that facilitates gradual cargo release. This release rate is controlled by the degree of ionization of CS's amine groups, which varies with local acidity.[29]

Curcumin (bis[4-hydroxy-3-methoxyphenyl]-1,6-heptadiene-3,5-dione)[30] (Scheme 1), the main component of turmeric, is derived from the rhizome of the Curcuma longa plant.[31] It has demonstrated anti-inflammatory properties.[32,33] The interest in curcumin as an anti-cancer agent arises from epidemiological evidence linking turmeric consumption to lower rates of gastrointestinal cancers. Experimental studies demonstrate that curcumin induces apoptosis in various cancer cell lines derived from solid tumors, including those of lung, colorectal, breast, pancreatic, and prostate cancers.[34] Furthermore, its metal-chelating ability suggests potential applications in treating metal toxicity.[35] Curcumin, an oil-soluble compound, is practically insoluble in water at neutral and acidic pH levels but soluble in alkali. It remains stable at high temperatures and in acidic conditions but becomes unstable when exposed to light.[36] Despite these promising properties, curcumin faces challenges due to its limited bioavailability when administered

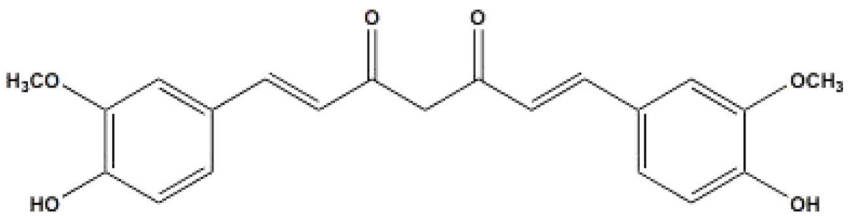

Scheme 1 Curcumin structure.

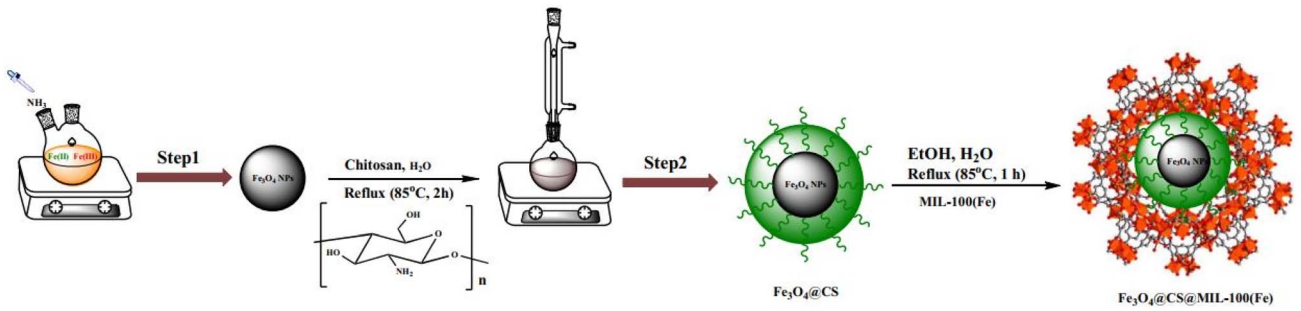

Scheme 2 Synthesis route of Fe_3O_4@CS/MIL-100(Fe).

orally. To address this issue, nanotechnological approaches have been explored to enhance curcumin delivery to target tissues.[37–39] Some recent evaluations have focused on core–shell structures, including MIL-100(Fe)@SiO_2, SiO_2@MIL-100(Fe)[40] and MIL-100(Fe)@carboxymethyl cellulose (CMC), as carriers for curcumin [41] Larasati *et al.* demonstrated high curcumin loading (up to 97.89%) and slow drug release from the protected core of MIL-100(Fe) under acidic conditions.[40] To the best of our knowledge, MIL-100(Fe) supported on magnetite-chitosan has not been investigated for drug delivery systems.

In targeted drug delivery, biocompatible nanocomposites play a crucial role in directing drugs to specific tissues while minimizing side effects. However, the SiO_2 used for magnetite coating is not biocompatible for MOF growth. In contrast, chitosan coating is entirely biocompatible, making the Fe_3O_4@CS substrate an ideal choice for growing MOF for drug delivery. To the best of our knowledge, MIL-100(Fe) supported on magnetite-chitosan has not been investigated for drug delivery systems, This study aims to bridge this gap by developing and characterizing a Fe_3O_4@chitosan/MIL-100(Fe) nanocomposite (denoted as FCM, Scheme 2) that enhances curcumin loading, stability, and targeted higher release compared to other curcumin delivery systems utilizing the same MOF while minimizing toxicity to normal cells. Our results demonstrate a high loading capacity for curcumin in a mixture of water and acetone (volume ratio 2 : 3) over 24 hours. Additionally, we observed

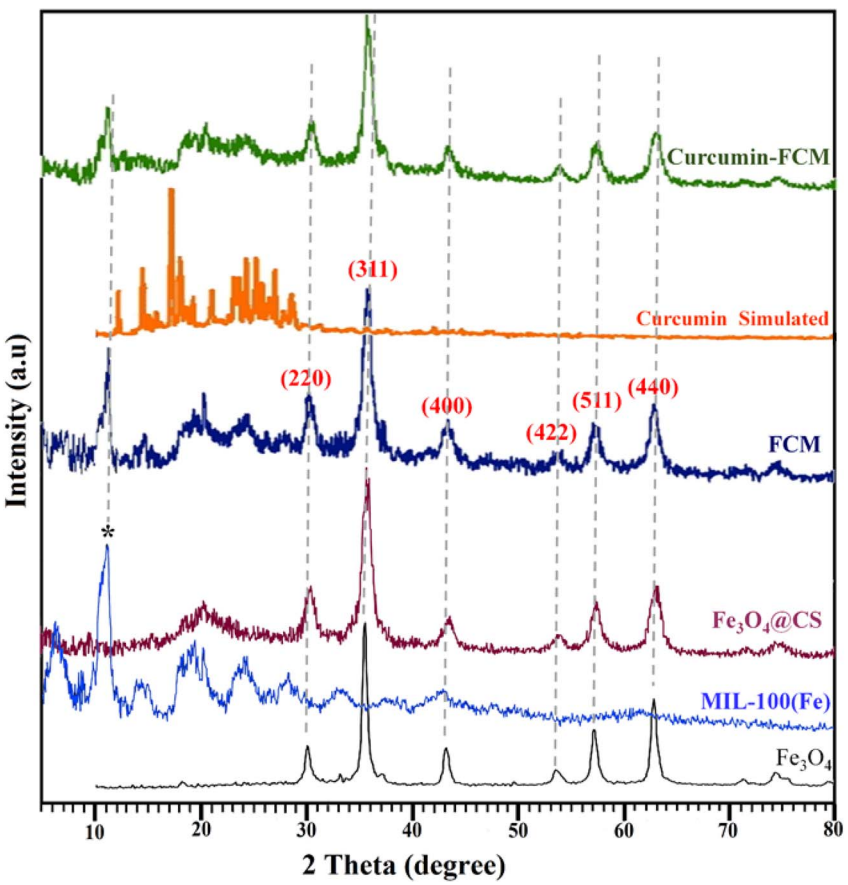

Fig. 1 XRD diffraction patterns of the MIL-100(Fe), Fe3O4@Cs, FCM and cucrumin-FCM.

controlled drug release in 0.1% and 0.2% Tween 80-buffer media at pH 7.4 and pH 5, respectively. MTT analysis confirmed the biocompatibility of the carrier composite with normal cell lines.

2 Experimental

2.1 Chemicals and instrumentations

All chemicals included ferrous chloride tetrahydrate, ferric chloride hexahydrate, acetone, ammonia, sodium hydroxide, trimesic acid, were purchased from Merck Co. (Germany) and Sigma-Aldrich (USA) and used without further purification. The pH meter (Starious, Germany) used for pH adjustment, Fourier transform infrared spectra (FT-IR) were recorded as KBr pellets using a PerkinElmer 781 spectrophotometer. X-ray powder diffraction (XRD) patterns of samples were obtained with a Philips Xpert X-ray powder diffractometer (Cu Kα radiation, $\lambda = 0.154056$ nm). UV-visible spectra were recorded in the range 200–800 nm on Photonix Ar 2015 UV-visible spectrophotometer. The structure and surface morphology of the prepared samples were investigated by field emission scanning electron microscope (FE-SEM ZEISS-Sigma-300). Zeta potential was measured using sz-100z (Horiba jobin jyovin, Japan). Magnetization curves were recorded by Meghnatis Daghigh Kavir Co Vibrating sample magnetometer (VSM) at room temperature. TGA-DTA curves were recorded by a Rheometric Scientific Inc. 1998 thermal analysis apparatus under a N_2 atmosphere. Nitrogen adsorption–desorption isotherms were measured at 196 °C using a Belsorp mini II (Microtrac Bel Crop Japan) automatic adsorption instrument after degassing the samples at 150 °C for 5 h.

2.2 Fabrication of Fe_3O_4 nano-particles (MNPs)

Fe_3O_4 NPs were synthesized using the co-precipitation method, as previously described in our works.[21,42,43] Initially, an aqueous solution containing Fe(II) and Fe(III) ions in a molar ratio of 1 : 2 was gradually heated to 80 °C. Subsequently, the pH was adjusted to 10 by alkalization, and the reaction was allowed to continue for two hours. The resulting sediment was collected, washed, and then dried at 60 °C for 12 hours.

2.3 Development of Fe_3O_4@CS core–shell

To grow chitosan polymer on magnetite nanoparticles, we adapted a method based on Van Hieu's work. An aqueous suspension of chitosan (0.1 g/10 mL) was added to ultrasonicated Fe_3O_4 powder (0.1 g/10 mL). The mixture was then refluxed for 2 hours at 80–85 °C. After refluxing, the product was separated using an external magnet, purified with ethanol and deionized water, and finally dried at room temperature.[44]

2.4. Preparation of MIL-100(Fe) and Fe_3O_4@Cs/MIL-100(Fe)

The synthesis of MIL-100(Fe) followed an established procedure. $Fe(NO_3)_3 \cdot 9H2O$ (1.01 g) and H3BTC (0.47 g) were added to a round-bottom flask containing 10 mL of deionized water. The mixture was refluxed with vigorous stirring at 85–90 °C for 8 hours, producing a dark orange deposit. This deposit was washed three times with ethanol and deionized water, then dried at 110 °C for 8 hours.[45,46] Subsequently, 0.1 g of MIL-100(Fe) was dispersed in 20 mL of ethanol and mixed with 0.1 g of sonicated Fe_3O_4 powder in 10 mL of deionized water while stirring. The resulting mixture was refluxed at 85 °C for one hour. The brown precipitate obtained was washed multiple times using an external magnet and dried at room temperature. This product is abbreviated as "FCM" in this manuscript.

2.5 Curcumin extraction

In accordance with previous studies,[47,48] To prepare the sample, 1 g of fine turmeric powder was gradually added to a 100 mL acetone solution while vigorously stirring for 48 hours in a closed container at room temperature, maintaining a dark environment. After centrifuging the mixture at 6000 rpm, the liquid portion above the sediment was carefully collected. This supernatant was subsequently transferred to a vacuum desiccator for drying, resulting in a red residue.

2.6 Evaluation loading and release of curcumin-loaded Fe_3O_4@Cs/MIL-100(Fe)

To maximize drug loading content and efficiency, we used 0.01 g of the drug with varying amounts of adsorbents (0.02, 0.025, 0.03, 0.035, 0.04, 0.045, and 0.05 g), all achieving a loading percentage above 97%. When the drug amount was increased to 0.02 g, the loading efficiency remained above 95% with the same adsorbent quantities. However, further increasing the drug amount resulted in a lower loading efficiency. A specific quantity of curcumin was initially dissolved in 2 mL of acetone and then diluted to 5 mL using deionized water. Additionally, chosen amount of FCM was introduced into the

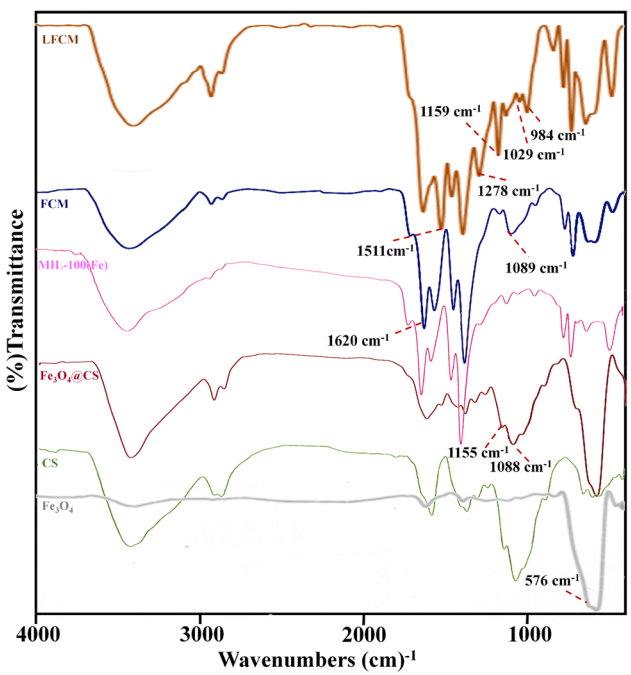

Fig. 2 FT-IR spectra of the Fe_3O_4, Chitosan (CS), Fe_3O_4@CS, MIL-100(Fe), FCM and LFCM.

curcumin solution. The reaction vessel was sealed in darkness, and stirring continued for 24 hours. Finally, the black precipitate, which is abbreviated as LFCM in this manuscript, obtained was dried at ambient temperature after thorough washing with deionized water and separation by centrifugation. The washing solution from this process was also utilized for the UV-vis spectrum analysis at $\lambda = 425$ nm, following the calibration curve, this curve is shown in Fig. S1 (ESI†), and for calculating drug loading efficiency (DLE), drug loading content (DLC), and drug loading capacity (q). These results were obtained using the specified formulas:[49,50]

$$\text{Drug loading efficiency(DLC)} = \frac{M_{\text{drug}}}{M_{\text{drug}} + M_{\text{excipient}}} \times 100\% \quad (1)$$

$$\text{Drug loading content(DLE)} = \frac{M_{\text{drug}}}{M_{\text{drugfeed}}} \times 100\% \quad (2)$$

$$q_e = (C_0 - C_e) \times \frac{V}{W} \quad (3)$$

M_{drug} and $M_{\text{excipient}}$ represent the mass of the loaded drug and FCM in the solution, respectively. $M_{\text{drug feed}}$ is the amount of drug feed in the provision of the LFCM formulation. C_0 and C_e (measured in mg L^{-1}) denote the initial and equilibrium concentrations of curcumin drug, V (L) is the volume of the solution, and W (g) is the mass of the MOF nanocomosite.

2.7 *In vitro* release studies of curcumin from LFCM

Curcumin release studies were conducted in 0.1% and 0.2% Tween 80-buffer media at pH 7.4 and pH 5. In this experimental setup, suspensions of loaded FCMs (0.03 g) were stirred in 200 mL of Tween 80-buffer media at 37 °C under dark conditions. At specified time intervals, 2 mL of supernatant fluid was withdrawn and transferred into centrifuge falcon tubes. The drug present in the separated samples was quantified by centrifugation at 6000 rpm for 5 minutes, followed by UV-visible spectrophotometry using calibration curves established in acetone and 0.1% to 0.2% Tween 80-buffer (Fig. S2 and S3†).

2.8. *In vitro* cytotoxicity assessment

The cytotoxicity effect of curcumine, FCM and LFCM was studied using the MTT assay. For this test, the Breast cancer cell line (MCF-7) and human dermal fibroblast cells (HDF) were obtained from the Pasteur Institute of Iran. The cells were

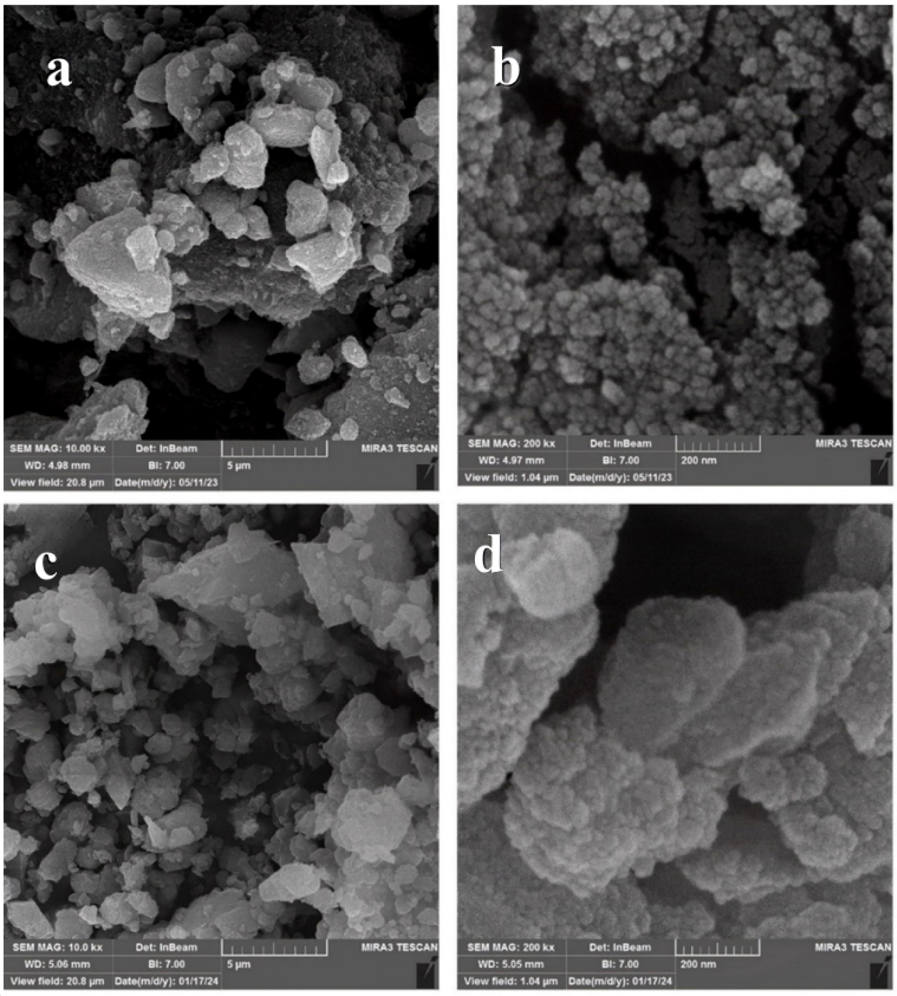

Fig. 3 FE-SEM images of Fe_3O_4@CS (a, b) and MIL-100(Fe) (c and d).

cultured in Dulbecco's Modified Eagle Medium (DMEM) with 10% Fetal Bovine Serum (FBS) growth media with with 100 U mL^{-1} penicillin–streptomycin. The cells were placed in an incubator with 95% humidity, 5% CO_2 concentration, and a temperature of 37 °C. The cytotoxicity of the treated cells was determined using the MTT test. First, 1×10^4 cells were seeded in a 96-well plate and incubated for 24 hours. After that, the cells were treated with FCM, curcumin, and LFCM at concentrations of 5, 10, 15, and 20 ppm. The plates were incubated at 37 °C for 24, 48, and 72 hours. Following the incubation time, the media was replaced with a new culture medium containing 10% MTT solution in PBS, and the plates were incubated at 37 °C for 3 hours. After that, 150 μL of DMSO was added to each well. The plates were placed on a shaker for 20 minutes to dissolve the formazan crystals in DMSO. The optical density was read at 570 nm using a microplate reader (BioTek ELX800, USA).

3 Results and discussion

3.1 Characterization

The powder X-ray diffraction (PXRD) structural patterns of FCM and Curcumin-FCM were compared with those of bare MIL-100(Fe) and Fe_3O_4@CS in Fig. 1. Representative peaks at 6.8°, 10.8°, 14.6°, 19°, 23.8°, and 27.9° correspond to MIL-100(Fe).[21,51] Notably, the prime peak of MIL-100(Fe) is visible, marked by a star (*) symbol, with a slight shift observed at 11.22° in FCM and 11.057° in Curcumin-FCM. In the PXRD pattern of Fe_3O_4@CS, a broad peak centered around 20.29° (attributed to chitosan)[52] appears alongside characteristic peaks at about 30.39°, 35.8°, 43.5°, 53.9°, 57.45°, and 63.09° corresponding to (2 2 0), (3 1 1), (4 0 0), (4 2 2), (5 1 1), and (4 4 0) respectively. The presence of these peaks at specific angles indicates that the sample has a well-defined crystal structure, confirming its identity as magnetite and the successful grafting of the polymer onto magnetite particles.[53] This presence signifies the successful grafting of the polymer onto magnetite particles. Interestingly, the concurrent peaks relevant to the MOF (Metal–Organic Framework) and chitosan-coated magnetite are evident in their composite structure. Furthermore, the remarkable crystallinity of FCM is maintained even after drug loading. However, in the PXRD pattern of curcumin-FCM, no distinctive peak corresponding to curcumin is observed.[54] Presumably, the drug is well dispersed within the FCM structure.

The FT-IR spectra of the magnetite, chitosan, magnetit-chitosan, MIL-100(Fe), FCM and LFCM has been shown in Fig. 2. As shown in the FT-IR spectrum of Fe_3O_4@CS, the

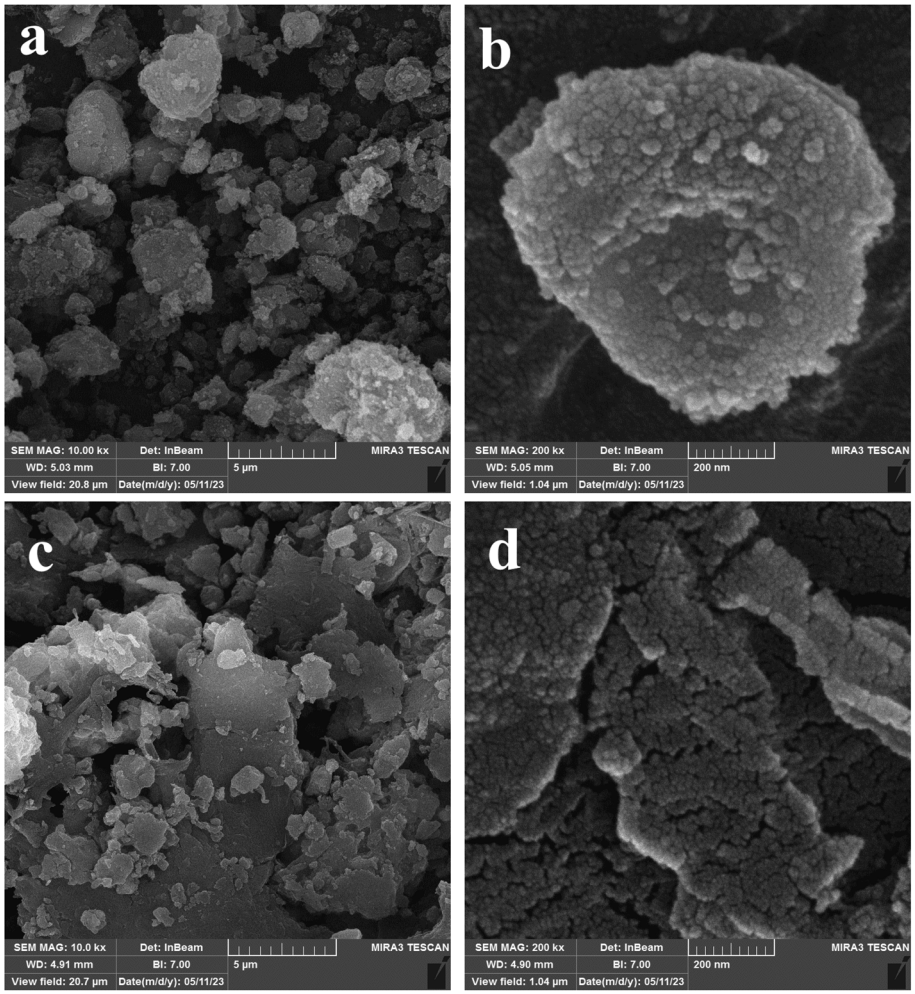

Fig. 4 FE-SEM images of FCM (a, b) and LFCM (c and d).

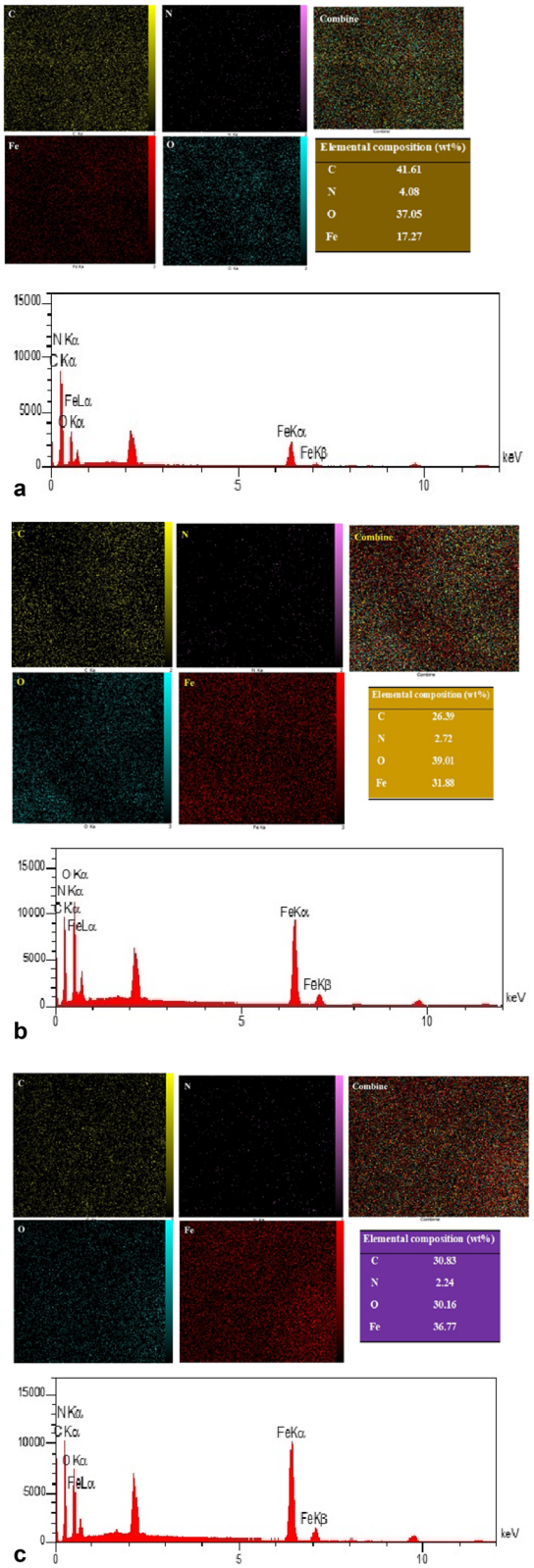

Fig. 5 (a) EDX spectrum of Fe_3O_4@CS and the corresponding elemental mappings for C, O, Fe and N elements. (b) EDX spectrum of FCM and the corresponding elemental mappings for C, O, Fe and N elements. (c) EDX spectrum of LFCM and the corresponding elemental mappings for C, O, Fe and N elements.

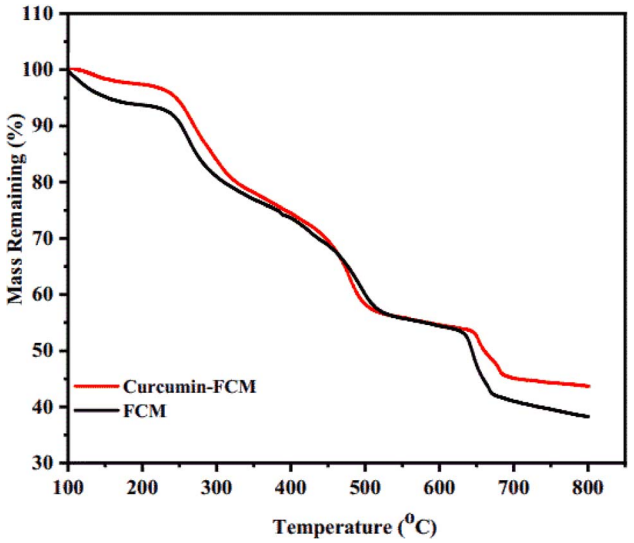

Fig. 6 TGA curves of LFCM and FCM.

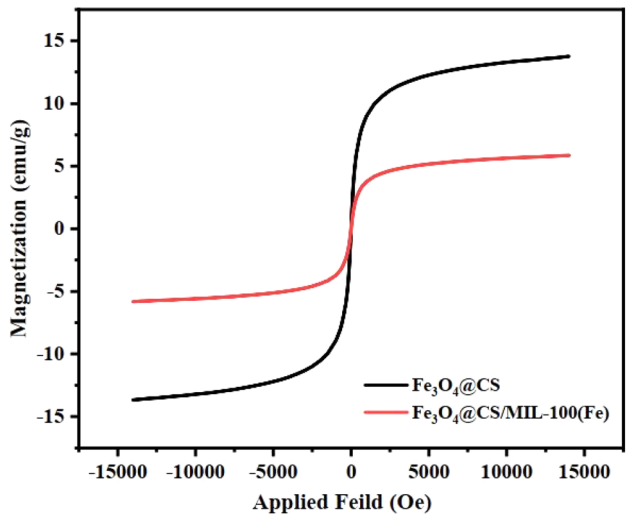

Fig. 7 Magnetization *versus* applied field (H) FC and FCM nanoparticles.

chitosan coating on magnetite nanoparticles results in the appearance of characteristic bands of chitosan with a slight upward shift compared to free chitosan. These absorption bands include C=O stretching at 1617 cm^{-1}, N–H bending at 1558 cm^{-1}, and C–N stretching at 1260 cm^{-1}, as well as –C–O– stretching of the primary alcoholic group at 1381 cm^{-1}, CH_2 bending at 1428 cm^{-1}, asymmetric and symmetric stretching of the –C–O–C– bridge at 1155 cm^{-1} and 1088 cm^{-1}, CH_2 aliphatic group stretching at 2860 cm^{-1} and 2921 cm^{-1}, and a broad band for –OH and –NH stretching at 3432 cm^{-1} (ref. 55 and 56) Additionally, the typical Fe_3O_4 band appears at 576 cm^{-1}. Upon introducing MIL-100(Fe) to the chitosan-magnetite, the intensity of the Fe–O band at 576 cm^{-1} decreases, and MIL-100(Fe) vibrations appear at 711 cm^{-1} and 761 cm^{-1}, attributed to –CH aromatic bending. However, the chitosan bands from

1260 cm^{-1} to 1617 cm^{-1} overlap with the sharp bands of MIL-100(Fe), corresponding to COO^- stretching vibrations at 1620 cm^{-1}, 1442 cm^{-1}, and 1372 cm^{-1}, as well as C=C aromatic ring vibrational bands at 1559 cm^{-1}.[57,58] The broad stretching band of the –C–O–C–bridge at 1089 cm^{-1} and the CH_2 aliphatic bands at 2860 cm^{-1} and 2921 cm^{-1} further assert the growing of MOF on the magnetite-chitosan.

The FT-IR spectrum analysis of extracted curcumin (Fig. S4†) revealed characteristic peaks of curcumin.[59] Notably, the absorption bands of curcumin, such as the stretching vibrations of C–O (1278 cm^{-1}), C–O–C (1029 cm^{-1}), and the bending bands of out-of-plane and in-plane C–H (984 $cm^{-1}$and 1159 cm^{-1}), are clearly visible in the spectrum of the drug-loaded MOF. In the LFCM spectrum, the blue-shift and decreased intensity of the bending vibration of curcumin (984 cm^{-1}) compared to free curcumin (967 cm^{-1}), along with the red-shifted FT-IR bands of MOF (1559 cm^{-1}) and the broadening of the absorption bands of MOF, indicate a restriction of movement due to the microporous host matrix and the influence of dispersion forces between the microporous host matrix and the guest molecules.[10]

The field-emission scanning electron microscopy (FESEM) images of Fe_3O_4@CS, pure MIL-100(Fe), and their merged nanocomposites are depicted in Fig. 3 and 4. Here's a breakdown of the observations: Fe_3O_4@Chitosan compound (Fig. 3a and b): agglomerations of spherical particles with a uniform size distribution are evident. The morphology suggests that Fe_3O_4@CS consists of well-defined particles. Pure MIL-100(Fe) (Fig. 4c and d): MIL-100(Fe) exhibits polydispersity, with aggregates of round-shaped particles smaller than 5 μm. The irregular particle arrangement is characteristic of MIL-100(Fe). Merged nanocomposites (Fig. 4a and b): after combining MOF (Metal–Organic Framework) and chitosan-containing magnetite, the MOF structure remains intact. Notably, spherical chitosan-magnetite particles are discernible on the surface of the MOF. Porous surfaces and drug loading: Fig. 4c and d reveal uniformly filled porous surfaces in the resulting nanocomposite after drug loading.

Energy-dispersive X-ray spectroscopy (EDX) patterns and corresponding elemental mappings for FC, FCM, and LFCM are shown in Fig. 5a–c. The EDX patterns confirm the presence of carbon (C), oxygen (O), iron (Fe), and nitrogen (N) in the FC, FCM, and LFCM samples. Additionally, the mapping analysis of nanoparticles reveals a uniform and homogeneous distribution of these elements. The elemental composition of FC primarily consists of carbon (Fig. 5a). Upon introducing MIL-100(Fe) onto chitosan-magnetite surfaces, the iron content increases (Fig. 5b). Notably, LFCM exhibits a higher carbon content compared to the drug-free MOF composite, likely due to the pores of the nanocomposite being filled with curcumin (Fig. 5c).

Thermogravimetric analysis (TGA) was performed on the samples to assess mass changes as a function of temperature, as illustrated in Fig. 6. This analysis offers valuable insights into the thermal stability, decomposition behavior, and the presence of organic or inorganic components in nanoparticles, which are critical factors influencing their safety and efficacy in drug delivery.

The mass loss of FCM occurs in four distinct stages: water removal from the pores (100–250 °C), simultaneous dehydroxylation of oxo-metals in MIL-100(Fe) and decomposition of unstable nitrogen and oxygen groups (250–350 °C), collapse of MIL-100(Fe) (350–500 °C), and thermal degradation of chitosan (300–400 °C).[60] The final weight loss (650–700 °C) corresponds to the complete decay of the organic ligand, leaving residual metal oxides. These results are consistent with previous studies.[61,62] The TGA curve for LFCM shows similar steps but with greater mass loss (5%) in the 200–500 °C range due to curcumin degradation.[63] Additionally, the curcumin composite has a higher residue (43.7%) compared to the free composite (38.7%), indicating enhanced thermal stability due to curcumin incorporation. These two differences confirm the successful incorporation of the drug into the adsorbent.

Magnetization studies are essential for evaluating the nanoparticles' responsiveness to magnetic fields, a key factor in targeted drug delivery systems, where external magnetic fields can direct the particles to specific sites in the body. Clarifying these properties ensures the nanoparticles are optimized for controlled, safe, and precise drug delivery. The magnetic behavior of the samples (FC and FCM) was confirmed using device magnetometry (vibrating sample magnetometry (VSM)), as shown in Fig. 7. The intersection of both curves at the zero point in the VSM plot signifies zero coercivity and confirms the presence of superparamagnetic properties. This superparamagnetic behavior arises from the nanoparticles' submicron size. The magnetic saturation (Ms) values for FC and FCM

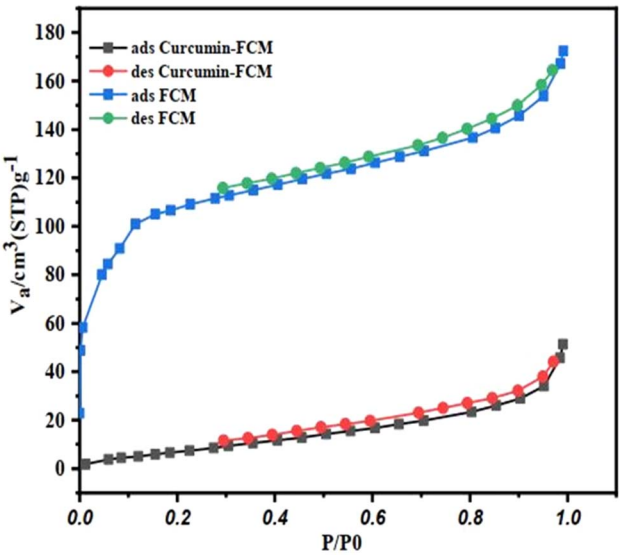

Fig. 8 Adsorption/desorption isotherms of FCM and LFCM.

Table 1 The parameters of BET and BJH for FCM and LFCM

Samples	BET surface area (m^2 g^{-1})	Average pore diameters (nm)	Total pore volume (cm^3 g^{-1})
FCM	431.22	2.4542	0.2646
Curcumin-FCM	34.484	9.1236	0.078655

were determined to be 13.75 emu g^{-1} and 5.86 emu g^{-1}, respectively. This phenomenon enables the Fe_3O_4@CS/MIL-100(Fe) nanoparticles to remain dispersed in water for several hours before gradually precipitating from the solution. These attributes are crucial for biomedical applications. Although coating FC on the dielectric MIL-100(Fe) reduced the superparamagnetic behavior, the Ms values are comparable to those reported in the literature for FC.[44,64,65] Magnetic separation and targeted drug delivery remain feasible.

Fig. 8 displays the N_2 adsorption/desorption isotherms for FCM and LFCM. The pore size distribution before and after drug loading have been shown in Fig. (S5).† Table 1 details the BET (Brunauer–Emmett–Teller) and BJH (Barrett–Joyner–Halenda) analyses for the synthesized samples. Initially, the nanocomposite without the drug showed a surface area of 431.22 m^2 g^{-1} and a pore volume of 0.2646 cm^3 g^{-1}. These values align with the IUPAC classification, where the adsorption isotherm corresponds to type II and an H4 hysteresis loop is observed. However, after drug loading, these values decreased to 34.484 m^2 g^{-1} and 0.078655 cm^3 g^{-1}, respectively. The isotherm shape in Fig. 8 corresponds to type III adsorption with an H3 hysteresis loop. These results confirm the successful loading of synthesized FCM with curcumin.

The surface charge of the synthesized samples, including FC, MIL-100(Fe), FCM, and LFCM, was determined in a water/ethanol medium (volume ratio of 1 : 2) using zeta potential measurements, as shown in Fig. 9. The mean zeta potential values were −9 mV for Fe_3O_4@CS, −17.9 mV for MIL-100(Fe), and −15.7 mV for Fe_3O_4@CS/MIL-100(Fe) (see Fig. 9). Notably, the negative surface charge of MIL-100(Fe) decreased to −15.7 mV after interacting with Fe_3O_4@CS, indicating the formation of the composite structure FCM. Additionally, under physiological conditions (pH 7.4), the surface charge of curcumin-loaded FCM was evaluated as 0.3 mV.

3.2 Adsorption of curcumin

Curcumin, though practically insoluble in water, shows good solubility in organic solvents (pH 1–7), alkali (pH > 7), and

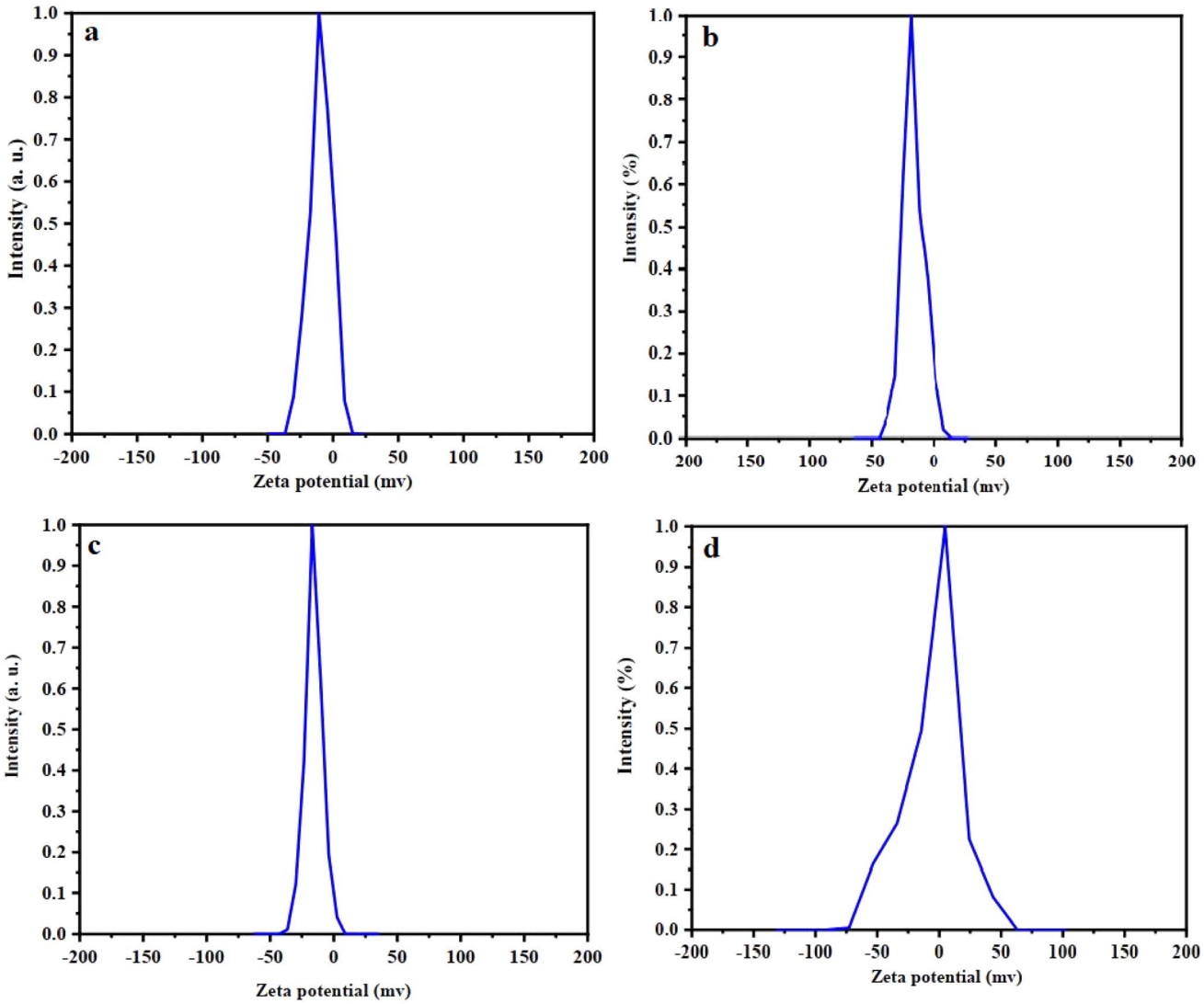

Fig. 9 Zeta potential curves of (a) FC, (b) MIL-100(Fe), (c) FCM and (d) LFCM.

strongly acidic media (pH < 1). It can exist in neutral, anionic, and cationic forms. Unfortunately, curcumin rapidly decomposes at pH values greater than 8.[66,67] To address this, drug adsorption studies were conducted using a water/acetone mixture. In this context, curcumin remains relatively neutral, and interactions such as dipole–dipole, dipole-ion, and hydrogen bonding with chitosan play crucial roles in drug adsorption.[40] Regarding drug loading, a survey was performed on MIL-100(Fe), Fe_3O_4@CS, and powder samples of FC/MIL-100(Fe) with varying mass ratios of FC to MIL-100(Fe). These samples are abbreviated as FCM-0.5, FCM-1.0, and FCM-2.0, respectively (see Fig. S6†). As can be seen from the images, the color becomes darker as the ratio of the metal–organic framework increases. Fig. 10 illustrates the loading profile of curcumin in the synthesized samples.

The experimental findings indicate that curcumin's encapsulation efficiency (EE) peaks at an equimolar (1 : 1) ratio of magnetite-chitosan to MIL-100(Fe). This superior performance is likely the result of a well-balanced interplay between structural and functional properties. At this ratio, MIL-100(Fe) provides a large surface area and hydrophobic cavities that promote effective curcumin encapsulation, while its exposed Fe^{3+} sites enhance molecular interactions. Chitosan contributes by improving dispersibility and ensuring colloidal stability, whereas magnetite enables magnetic targeting without disrupting the porous structure of the MOF. Deviating from this ratio leads to undesirable effects, such as pore blockage (due to excess magnetite-chitosan) or reduced stability (from excess MIL-100), ultimately lowering the encapsulation efficiency. Therefore, the 1 : 1 ratio emerges as the optimal composition for effective curcumin delivery in targeted therapeutic applications.

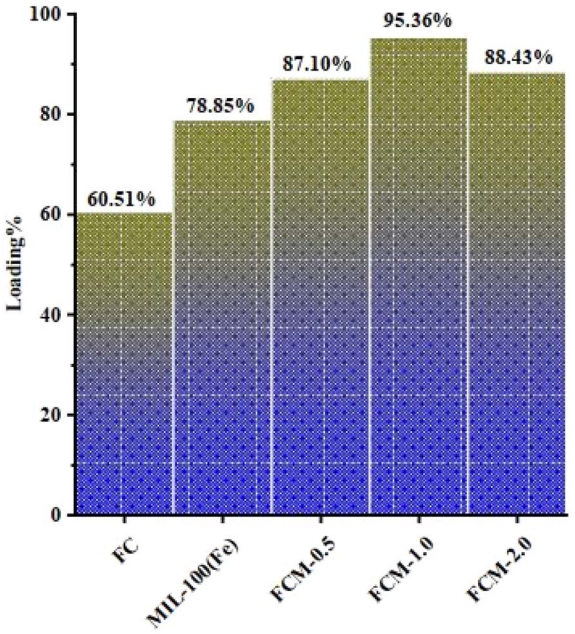

Fig. 10 Curcumin encapsulation efficiency (%) of the FC, MIL-100(Fe), FC/MIL-100(0.5), FC/MIL-100(1.0), FC/MIL-100(2.0).

3.3 Isotherm and kinetic modeling of adsorption

Curcumin adsorption isotherm experiments were conducted using 0.01 g of FCM by adding 10 mL of various initial drug concentrations ranging from 12.5 ppm to 600 ppm in a water/acetone mixture. After sufficient time under dark conditions, the capacity and equilibrium concentrations were calculated. The investigated equations, including Langmuir, Freundlich, Temkin, Dubinin–Radushkevich, and Redlich–Peterson, are respectively expressed by the following formulas:

$$\frac{C_e}{q_e} = \frac{C_e}{q_{max}} + \frac{1}{k_L q_{max}} \quad (4)$$

$$q_e = K_F (C_e)^{1/n} \quad (5)$$

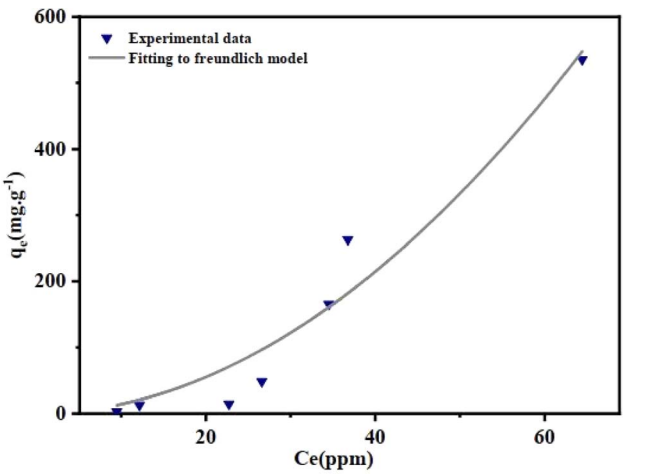

Fig. 11 The loading curve for curcumin adsorption onto the FC/MIL-100(Fe) nanocomposite and the corresponding Freundlich adsorption model.

Table 2 Parametrs and regression coefficients for isotherm adsorbsion models

Isotherm	Equation	Parameters
Langmuir	$\frac{C_e}{q_e} = \frac{C_e}{q_{max}} + \frac{1}{k_L q_{max}}$	$K_L = 0.019$, $R^2 = 0.49$
Freundlich	$q_e = K_F (C_e)^{1/n}$	$n = 0.51$, $K_F = 0.154$, $R^2 = 0.95$
Temkin	$q_e = B \quad \ln(K_T) + B \quad \ln(C_e)$	$B = 252.228$, $K_T = 13.708$, $R^2 = 0.72$
Dubinin–Radushkevich	$\ln(q_e) = \ln(X_m) - \beta\varepsilon^2$	$E = 1.43 \times 10^{-4}$ (Kj mol^{-1}), $R^2 = 0.83$
Redlich–Peterson	$\mathrm{Ln}\left(\frac{C_e}{q_e}\right) = \beta \ln C_e - \ln A$	$\beta = -1.7$, $a = 119.1$, $R^2 = 0.80$

Table 3 Adsorption kinetic equations of FCM

Kinetic model	Equation	Parameters
Pseudo-first-order	$q_t = q_e\,(1-\exp(-k_1 t))$	$q_e = 55.23$, $k_1 = 1.85\times 10^2$, $R^2 = 7.21645 \times 10^{-15}$
Pseudo-second-order	Type(1): $\frac{t}{q_t} = \frac{1}{k_2 q_e^2} + \frac{1}{q_e}(t)$	$q_e = 86.2$, $k_2 = 1.35 \times 10^{-4}$, $R^2 = 0.98$
	Type(2): $\frac{t}{q_t} = \frac{1}{q_e} + \frac{1}{k_2 q_e^2}\left(\frac{1}{t}\right)$	$q_e = 59.17$, $k_2 = 1.3 \times 10^{-3}$, $R^2 = 0.61$
	Type(3): $q_t = q_e - \frac{1}{k_2 q_e}\left(\frac{q_t}{t}\right)$	$q_e = 63.33$, $k_2 = 9.7 \times 10^{-4}$, $R^2 = 0.45$
	Type(4): $\frac{q_t}{t} = k_2 q_e^2 - k_2 q_e (q_t)$	$q_e = 73.12$, $k_2 = 3.8 \times 10^{-4}$, $R^2 = 0.45$
Elovich	$q_t = \frac{1}{\beta}\ln(\alpha\beta) + \frac{1}{\beta}\ln(t)$	$\alpha = 39.078$, $\beta = 0.0729$, $R^2 = 0.90$
Intra-particle diffusion	$q_t = K_{id}(t)^{0.5} + C$	$K = 2.506$, $C = 19.33$, $R^2 = 0.99$

$$q_e = B \quad \ln(K_T) + B \quad \ln(C_e) \tag{6}$$

$$\ln(q_e) = \ln(X_m) - \beta\varepsilon^2 \tag{7}$$

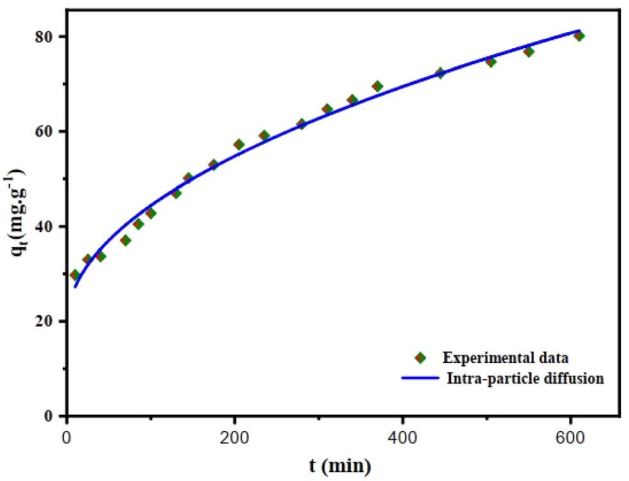

Fig. 12 Adsorption kinetic curve for curcumin adsorption onto the FC/MIL-100(Fe) nanocomposite and Intra-particle diffusion.

$$\mathrm{Ln}\left(\frac{C_e}{q_e}\right) = \beta \ln C_e - \ln A \tag{8}$$

In which C_e (mg L^{-1}), q_e (mg g^{-1}) and q_{max} (mg g^{-1}) are the equilibrium concentration of curcumin, the equilibrium adsorption capacity, and the maximum adsorption capacity of FCM, respectively. K_L (L mg^{-1}), K_F (mg g^{-1}) (L mg^{-1})$^{1/n}$, and K_{DR} (mol^2 kJ^{-2}) are equilibrium constants for Langmuir, Freundlich, and D-R isotherm models, respectively. Also R (8.314 J mol K^{-1}), T (K), and B are the gas constant, temperature, and constant relevant to the heat of adsorption, respectively. Moreover, ε (kJ mol^{-1}) denotes the Polanyi potential and n is the surface heterogeneity factor. Table 2 shows the parametrs and regression coefficients for isotherm adsorbsion models. According to Table 2, the only relatively suitable fitting data is related to the Freundlich equation (Fig. 11). The Freundlich adsorption isotherm characterizes adsorption on heterogeneous surfaces, indicating that active sites possess varying energy levels. Initially, high-energy sites become occupied, followed by those with lower energy. At elevated adsorbate concentrations, all active sites may become saturated, reaching maximum adsorption capacity. This model also allows for

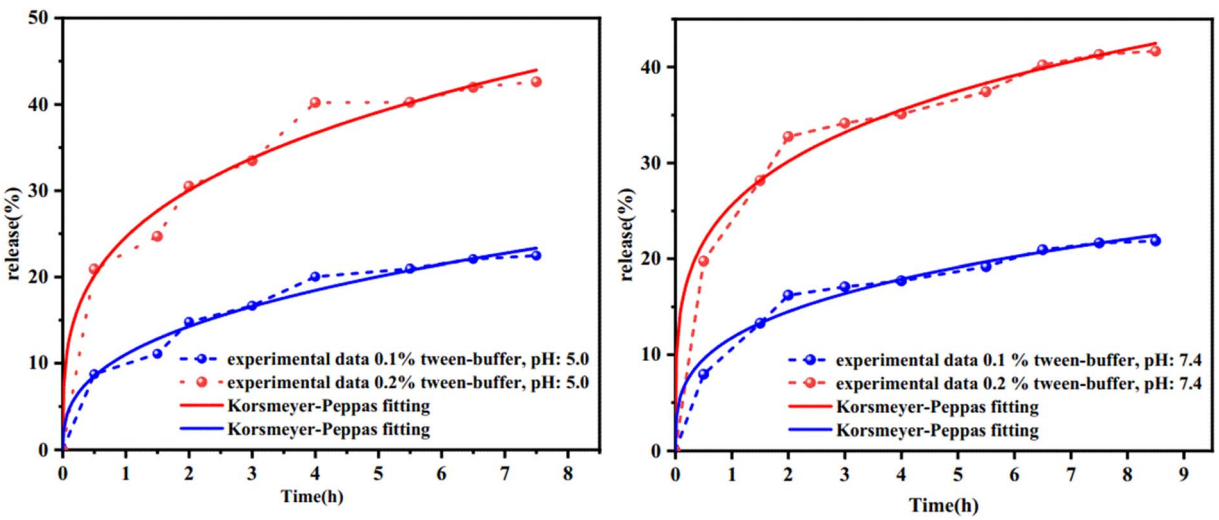

Fig. 13 The release of curcumin adsorption onto the FC/MIL-100(Fe) at pH 7.4 and pH 5.

multilayer adsorption. Conversely, the Langmuir isotherm assumes a homogeneous adsorbent surface with uniform energy sites, leading to monolayer adsorption. In the Freundlich model, the parameter (n) reflects adsorption intensity; n is a dimensionless parameter whose value is between 0 and 1 (n = 0.51) indicating as the adsorbate concentration increases, the adsorption capacity rises, albeit at a diminishing rate.[50]

The kinetics of adsorption was investigated with a 25 ppm mixture water/acetone of drug at different contact times of 10–610 minutes. The results of analyzed kinetic models such as pseudo-first order, pseudo-second order, Intra-particle diffusion, and Elovich are listed in Table 3. In these formulas, k is the adsorption rate constant, α (mg g^{-1} min) and β (g mg^{-1}) are the initial rate constants of adsorption and desorption. Adsorption kinetic curve of FCM is shown in Fig. 12. The intra-particle diffusion model focuses on the diffusion of the adsorbate within the adsorbent particles, suggesting that the rate-limiting step in adsorption is the movement of adsorbate molecules into the internal structure of the adsorbent.[68] In contrast, models such as pseudo-first-order, pseudo-second-order, and Elovich are primarily concerned with surface reaction mechanisms. The pseudo-first-order model assumes that the adsorption rate is proportional to the difference between the equilibrium adsorption capacity and the amount adsorbed at any time, indicating that the adsorption rate decreases as the surface sites become occupied. The pseudo-second-order model posits that the adsorption rate is proportional to the square of the difference between the equilibrium capacity and the amount adsorbed, suggesting that the adsorption rate decreases more rapidly as the surface sites become occupied.[69] The Elovich model is often used to describe adsorption on heterogeneous surfaces, where the rate of adsorption decreases exponentially with the amount adsorbed, reflecting a range of adsorption site energies.[70] A good fit of the intra-particle diffusion model to experimental data indicates that the rate-limiting step of adsorption is the diffusion of adsorbate molecules into the internal structure of the adsorbent particles.

3.4 Curcumin release

Curcumin release assessment was conducted using 0.1% and 0.2% Tween 80-buffer solutions at pH 7.4 and 5.0. Fig. 13 illustrates the controlled release profile of curcumin in the aforementioned media. Equilibrium occurs within 7.5 and 8.5 hours under acidic and physiological conditions for the 0.2% Tween solution, respectively, with a burst release observed within 2 hours (approximately 30%). Subsequently, the

Table 4 Kinetic parametrs of curcumin release

Zero-order R^2 K_O (h^{-1})	First- order R^2 K_1 (h^{-1})	Higuchi model R^2 K_H (h$^{-1/2}$)	Kor'peppas R^2 K_{kp} (h^{-n}) ^{n}
0.1% tween-pH: 7.4 0.74 1.99	0.71 0.096	0.96 7.23	0.96 11.76 0.3
0.2% tween-pH: 7.4 0.66 3.49	0.75 0.0728	0.94 11.5	0.97 25.6 0.24
0.1% tween-pH: 5.0 0.81 2.5	0.83 0.0127	0.93 5.79	0.96 11.02 0.37
0.2% tween-pH: 5.0 0.73 4.4	0.83 0.097	0.93 9.12	0.95 24.6 0.29

Table 5 Comparison of the release of the curcumin with other reported nanocarriers

Nanocarrier	Drug loading	Drug release (%)	Release time	Ref.
MIL-100(Fe)@SiO_2	Drug encapsulation efficiency: 97.8%	0.1% Tween-PBS at pH 7.4: ~2.5 0.1% Tween-PBS at pH 5.8: <5	250 min 300 min	40
SiO_2@MIL-100(Fe)	Drug encapsulation efficiency: 97.9%	0.1% Tween-PBS at pH 7.4: ~0 0.1% Tween-PBS At pH 5.8: ~5	250 min 300 min	40
MIL-100(Fe)	Drug loading efficiency:792.324 (mg g^{-1})	0.1% Tween -PBS at pH 7.4 : 40.1 0.1% Tween -PBS at pH 5.8 : 82.21	48 hours	41
MIL-100(Fe)@CMC	Drug loading capacity: 19.267 (mg g^{-1})	0.1% Tween-PBS at pH 7.4 : 7.6 0.1% Tween-PBS at pH 5.8 : 5.9	48 hours	41
MIL-101(Fe)	Drug loading content: 56.3%	0.1% Tween-PBS at pH 7.4 : 26 0.1% Tween-PBS at pH 5 : 64.7	22 days	72
β-CD-MOF	Encapsulation efficiency: 79.24%	pH 7.4 PBS: 13.12 pH 5.5 : 74.46	72 hours	73
Glutamine- β-CD-MOF	Encapsulation efficiency: 83.45%	pH 7.4 PBS: 8.68 pH 5.5 : 62.14	72 hours	73
Lf-CMD-CS-CUR@Eu-MOF	Entrapment efficiency: 88.87% Drug content: 3.45%	pH 5.8 : 78.12 pH 7.4 : 44.56	120 hours	74
CS-Fe_3O_4-RGO	Drug loading: 63% entrapment efficiency: 95.5%	pH 5.4 : 96 pH 7.4 : 40	72 hours	75
Fe_3O_4@CS/MIL-100(Fe)	Drug loading effectively%: 95.36	0.1% Tween-buffer at pH 7.4 : 21.8 0.2% Tween-buffer at pH 7.4 : 41.6 0.1% Tween-buffer at pH 5 : 22.45 0.2% Tween-buffer at pH 5 : 42.6	8.5 hours 7.5 hours	This work

maximum drug release reaches 42.6% and 41.65%, which is approximately twice the amount released in the 0.1% Tween solution. These findings suggest that in media where curcumin is neutral (pH 1–7), drug delivery is independent of pH and primarily dependent on drug solubility.

To understand the release mechanism of curcumin from the FCM formulation, various kinetic models, including Zero-Order, First-Order, Higuchi, and Korsmeyer–Peppas, were examined. The kinetic parameters of curcumin release are shown in Table 4. Based on this table, the Korsmeyer–Peppas kinetic model was found to be the most suitable for describing the release behavior of curcumin from FCM. Additionally, according to the Korsmeyer–Peppas model, the value of 'n' is less than 0.5, indicating Fickian drug diffusion.[71]

The efficiency of FCM was compared with other systems used for curcumin loading and release. Table 5 provides general information about other metal–organic frameworks used for curcumin release. According to this table, FCM demonstrates better efficiency than β-CD-MOF, and Glutamine-β-CD-MOF. It is comparable to nanocarriers such as MIL-100(Fe), MIL-100(Fe) @SiO_2 and SiO_2@MIL-100(Fe). On the other hand, the drug loading content is higher than that of Lf-CMD-CS-CUR@Eu-

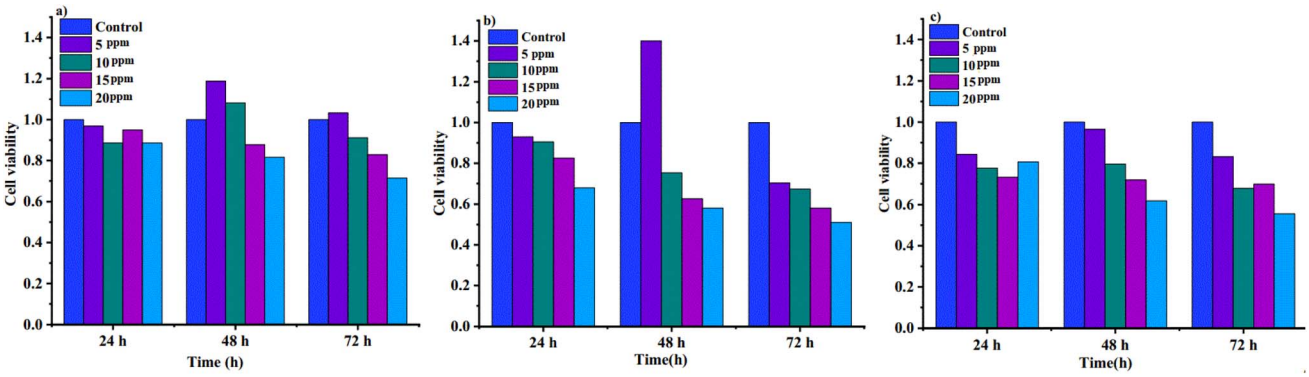

Fig. 14 MTT assay results for samples: viabilities of normal cells in the presence of (a) MOF, (b) curcumin, and (c) LFCM.

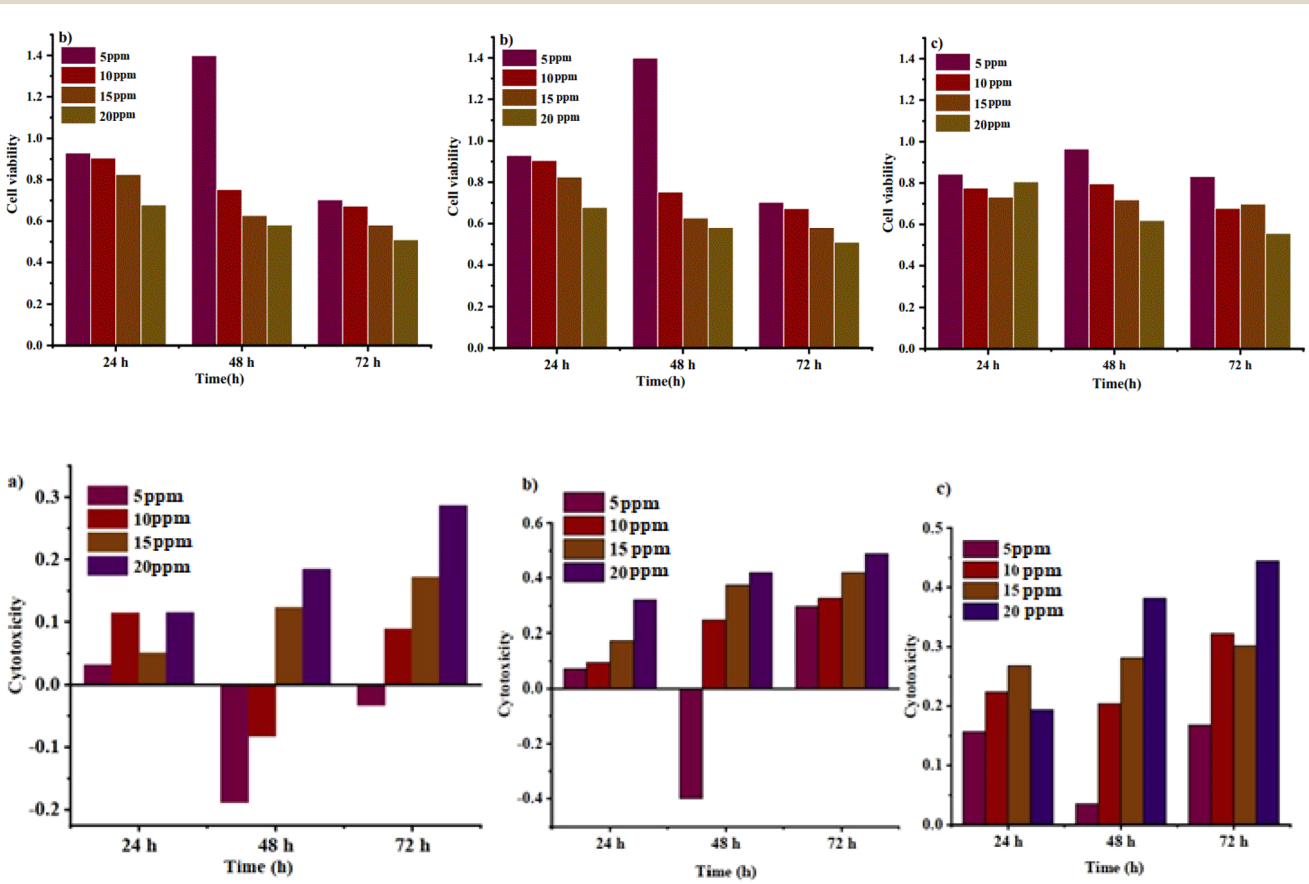

Fig. 15 Cell viability and cytotoxicity on MCF-7 cells in the presence (a) FCM, (b) curcumin and (c) LFCM.

MOF and MIL-100(Fe)@CMC compounds, and the drug is released in a shorter time.

3.5 Cytotoxicity assay

We investigated the toxicity of curcumin, the adsorbent (FCM), and the drug-loaded adsorbent (LFCM) toward HDF (Human Dermal Fibroblast) cells as normal cells and MCF-7 cancer cells. The experiments were conducted using volumes ranging from 5 to 20 ppm over periods of 24, 48, and 72 hours. The results, based on optical density and viability measurements, confirmed the high biological stability of the normal cell line with all samples, particularly at the 24- and 48 hour time points (as shown in Fig. 14). Interestingly, the drug-loaded metal–organic framework (MOF) demonstrated greater effectiveness against cancer cells compared to the free MOF and the drug alone. The cytotoxicity results against the MCF-7 line are significant at low concentrations compared to β-CD-MOF@CCM, glutamine-β-CD-MOF@CCM, and CCM-β-CD-MOF, Gelatin-β-CD-MOF@CCM and Gelatin nanoparticles systems studied so far. This suggests its potential as a promising drug delivery system (Fig. 15).

4. Conclusion

In this study, a novel magnetic nanocomposite (Fe_3O_4@CS/MIL-100(Fe)) was successfully synthesized and used as an effective nanocarrier for the loading and release of curcumin. The nanocomposite was characterized using various techniques, including FT-IR, FE-SEM, EDX, EDX-map, XRD, BET, TGA, and VSM. The drug loading efficiency reached 95.36% at a 1 : 1 ratio of Fe_3O_4@CS to MIL-100(Fe), and the Freundlich isotherm model best represented the adsorption data. The desorption kinetics followed the intra-particle diffusion model. The maximum drug release of about 40%, described by the Korsmeyer–Peppas model, occurred in both acidic and physiological environments. The drug-loaded nanocarrier showed high toxicity against MCF-7 breast cancer cells, while exhibiting less cytotoxicity towards human dermal fibroblast (HDF) cells, as confirmed by MTT analysis. Therefore, the high viability with normal cells and appreciable toxicity of the drug-loaded composite against cancer cells compared to the free drug and composite paves the way for future *in vivo* studies of this sparingly soluble drug.

Data availability

The authors confirm that the data supporting the findings of this study are available within the article.

Conflicts of interest

There are no conflicts to declare.

References

1 O. Afzal, A. S. Altamimi, M. S. Nadeem, S. I. Alzarea, W. H. Almalki, A. Tariq, B. Mubeen, B. N. Murtaza, S. Iftikhar, N. Riaz and I. Kazmi, Nanoparticles in Drug Delivery: From History to Therapeutic Applications, *Nanomaterials*, 2022, **12**, 4494.
2 M. K. Alshammari, M. M. Alshehri, A. M. Alshehri, O. M. Alshlali, A. M. Mahzari, H. H. Almalki, O. Y. Kulaybi, M. K. Alghazwni, M. Kamal and M. Imran, sparingly Camptothecin loaded nano-delivery systems in the cancer therapeutic domains: A critical examination of the literature, *J. Drug Delivery Sci.Technol.*, 2023, **79**, 104034.
3 C. Ma, Y. Peng, H. Li and W. Chen, Organ-on-a-chip: a new paradigm for drug development, *Trends Pharmacol. Sci.*, 2021, **42**, 119–133.
4 Y. Su, Z. Xie, G. B. Kim, C. Dong and J. Yang, Design strategies and applications of circulating cell-mediated drug delivery systems, *ACS Biomater. Sci. Eng.*, 2015, **1**, 201–217.
5 B. Bensaude Vincent and S. Loeve, Metaphors in nanomedicine: The case of targeted drug delivery, *NanoEthics*, 2014, **8**, 1–17.
6 P. Horcajada, R. Gref, T. Baati, P. K. Allan, G. Maurin, P. Couvreur, G. Ferey, R. E. Morris and C. Serre, Metal–organic frameworks in biomedicine, *Chem. Rev.*, 2012, **112**, 1232–1268.
7 I. Christodoulou, C. Serre and R. Gref, Metal-organic frameworks for drug delivery: Degradation mechanism and *in vivo* fate, *Met.-organ. Frameworks Biomed. Appl.*, 2020, 467–489.
8 X. Liu, T. Liang, R. Zhang, Q. Ding, S. Wu, C. Li, Y. Lin, Y. Ye, Z. Zhong and M. Zhou, Iron-based metal–organic frameworks in drug delivery and biomedicine, *ACS Appl. Mater. Interfaces*, 2021, **13**, 9643–9655.
9 B. Singco, L. H. Liu, Y. T. Chen, Y. H. Shih, H. Y. Huang and C. H. Lin, Approaches to drug delivery: Confinement of aspirin in MIL-100 (Fe) and aspirin in the *de novo* synthesis of metal–organic frameworks, *Microporous Mesoporous Mater.*, 2016, **223**, 254–260.
10 W. Strzempek, E. Menaszek and B. Gil, Fe-MIL-100 as drug delivery system for asthma and chronic obstructive pulmonary disease treatment and diagnosis, *Microporous Mesoporous Mater.*, 2019, **280**, 264–270.
11 L. Blaney, Magnetite (Fe_3O_4): Properties, synthesis, and applications, *The Lehigh Review*, 2007, **15**, 33–81.
12 L. Zhang, W.-F. Dong and H.-B. Sun, Multifunctional superparamagnetic iron oxide nanoparticles: design, synthesis and biomedical photonic applications, *Nanoscale*, 2013, **5**, 7664–7684.
13 H. Zhao, K. Saatchi and U. O. Hafeli, Preparation of biodegradable magnetic microspheres with poly (lactic acid)-coated magnetite, *J. Magn. Magn. Mater.*, 2009, **321**, 1356–1363.
14 Y. P. Yew, K. Shameli, M. Miyake, N. B. Khairudin, S. E. Mohamad, T. Naiki and K. X. Lee, Green biosynthesis of superparamagnetic magnetite Fe_3O_4 nanoparticles and biomedical applications in targeted anticancer drug delivery system: A review, *Arabian J. Chem.*, 2020, **13**, 2287–2308.

15 S. Mahmoudi, M. J. Chaichi, M. Shamsipur, O. L. Nazari and A. R. S. Maybodi, Modification of bimetal Zn/Mg MOF with nanoparticles Fe_3O_4 and Fe_3O_4@ SiO_2, investigation of the peroxidase-like activity of these compounds by calorimetry and fluorimetry methods, *Heliyon*, 2023, **9**, 1–14.

16 A. Bhattacharjee, S. Gumma and M. K. Purkait, Fe_3O_4 promoted metal organic framework MIL-100 (Fe) for the controlled release of doxorubicin hydrochloride, *Microporous Mesoporous Mater.*, 2018, **259**, 203–210.

17 H. Xu, H. Shi, Y. Yang and X. Liu, X., Synthesis and characterization of nanocomposites Fe_3O_4–SiO_2–chitosan based on lbl technology, *Glass Phys.Chem.*, 2016, **42**, 312–321.

18 A. Lajevardi, M. H. Sadr, M. T. Yaraki, A. Badiei and M. Armaghan, A pH-responsive and magnetic Fe_3O_4@ silica@ MIL-100 (Fe)/β-CD nanocomposite as a drug nanocarrier: loading and release study of cephalexin, *New J. Chem.*, 2018, **42**, 9690–9701.

19 A. Lajevardi, M. H. Sadr, A. Badiei and M. Armaghan, Synthesis and characterization of Fe_3O_4@ SiO_2@ MIL-100 (Fe) nanocomposite: A nanocarrier for loading and release of celecoxib, *J. Mol. Liq.*, 2020, **307**, 112996.

20 X. Ke, X. Song, N. Qin, Y. Cai and F. Ke, Rational synthesis of magnetic Fe 3 O 4@ MOF nanoparticles for sustained drug delivery, *J. Porous Mater.*, 2019, **26**, 813–818.

21 F. Parsa, M. Setoodehkhah and S. M. Atyabi, Loading and release study of ciprofloxacin from silica-coated magnetite modified by iron-based metal-organic framework (MOF) as a nonocarrier in targeted drug delivery system, *Inorg. Chem. Commun.*, 2023, **155**, 111056.

22 L. Li, S. Han, S. Zhao, X. Li, B. Liu and Y. Liu, Chitosan modified metal–organic frameworks as a promising carrier for oral drug delivery, *RSC Adv.*, 2020, **10**, 45130–45138.

23 T. Hidalgo, M. Giménez-Marques, E. Bellido, J. Avila, M. C. Asensio, F. Salles, M. V. Lozano, M. Guillevic, S.-R. Vazquez, A. Gonzalez-Fernández and C. Serre, Chitosan-coated mesoporous MIL-100 (Fe) nanoparticles as improved bio-compatible oral nanocarriers, *Sci. Rep.*, 2017, **7**, 43099.

24 L. A. Frank, G. R. Onzi, A. S. Morawski, A. R. Pohlmann, S. S. Guterres and R. V. Contri, Chitosan as a coating material for nanoparticles intended for biomedical applications, *React. Funct. Polym.*, 2020, **147**, 104459.

25 A. K. Resen, A. Atiroğlu, V. Atiroğlu, G. G. Eskiler, I. H. Aziz, S. Kaleli and M. Ozacar, Effectiveness of 5-Fluorouracil and gemcitabine hydrochloride loaded iron-based chitosan-coated MIL-100 composite as an advanced, biocompatible, pH-sensitive and smart drug delivery system on breast cancer therapy, *Int. J. Biol. Macromol.*, 2022, **198**, 175–186.

26 V. Mikušová and P. Mikuš, Advances in chitosan-based nanoparticles for drug delivery, *Int. J. Mol. Sci.*, 2021, **22**, 9652.

27 R. Abazari, A. R. Mahjoub, F. Ataei, A. Morsali, C. L. Carpenter-Warren, K. Mehdizadeh and A. M. Slawin, Chitosan immobilization on bio-MOF nanostructures: a biocompatible pH-responsive nanocarrier for doxorubicin release on MCF-7 cell lines of human breast cancer, *Inorg. Chem.*, 2018, **57**, 13364–13379.

28 M. Pooresmaeil, E. A. Asl and H. Namazi, A new pH-sensitive CS/Zn-MOF@ GO ternary hybrid compound as a biofriendly and implantable platform for prolonged 5-Fluorouracil delivery to human breast cancer cells, *J. Alloys Compd.*, 2021, **885**, 160992.

29 B. Ma, Q. Li, Y. Mi, J. Zhang, W. Tan and Z. Guo, pH-responsive nanogels with enhanced antioxidant and antitumor activities on drug delivery and smart drug release, *Int. J. Biol. Macromol.*, 2024, **257**, 128590.

30 E. H. Ismail, D. Y. Sabry, H. Mahdy and M. H. H. Khalil, Synthesis and Characterization of some Ternary Metal Complexes of Curcumin with 1, 10-phenanthroline and their Anticancer Applications, *J. Sci. Res.*, 2014, **6**, 509–519.

31 J. S. Jurenka, Anti-inflammatory properties of curcumin, a major constituent of Curcuma longa: a review of preclinical and clinical research, *Alternative Med. Rev.*, 2009, **14**, 141–153.

32 A. B. Kunnumakkara, D. Bordoloi, C. Harsha, K. Banik, S. C. Gupta and B. B. Aggarwal, Curcumin mediates anticancer effects by modulating multiple cell signaling pathways, *Clin. Sci.*, 2017, **131**, 1781–1799.

33 K. L. Priyadarsini, The chemistry of curcumin: from extraction to therapeutic agent, *Molecules*, 2014, **19**, 20091–20112.

34 R. Sinha, D. E. Anderson, S. S. McDonald and P. Greenwald, Cancer risk and diet in India, *J. postgrad. med.*, 2003, **49**, 222.

35 M. Borsari, E. Ferrari, R. Grandi and M. Saladini, Curcuminoids as potential new iron-chelating agents: spectroscopic, polarographic and potentiometric study on their Fe (III) complexing ability, *Inorg. Chim. Acta*, 2002, **328**, 61–68.

36 B. Zheng and D. J. McClements, Formulation of more efficacious curcumin delivery systems using colloid science: enhanced solubility, stability, and bioavailability, *Molecules*, 2020, **25**, 2791.

37 K. Gayathri, M. Bhaskaran, C. Selvam and R. Thilagavathi, Nano formulation approaches for curcumin delivery-a review, *J. Drug Delivery Sci. Technol.*, 2023, **82**, 104326.

38 S. I. Sohn, A. Priya, B. Balasubramaniam, P. Muthuramalingam, C. Sivasankar, A. Selvaraj, A. Valliammai, R. Jothi and S. Pandian, Biomedical applications and bioavailability of curcumin—An updated overview, *Pharmaceutics*, 2021, **13**, 2102.

39 R. Tabanelli, S. Brogi and V. Calderone, Improving curcumin bioavailability: Current strategies and future perspectives, *Pharmaceutics*, 2021, **13**, 1715.

40 N. Faaizatunnisa, W. W. Lestari, O. A. Saputra, T. E. Saraswati, L. Larasati and F. R. Wibowo, Slow-release of curcumin induced by core–shell mesoporous silica nanoparticles (MSNs) modified MIL-100 (Fe) composite, *J. Inorg. Organomet. Polym. Mater.*, 2022, **32**, 1744–1754.

41 A. Amalia, W. W. Lestari, J. H. Pratama, F. R. Wibowo, L. Larasati and T. E. Saraswati, Modification of dry-gel synthesized MIL-100 (Fe) with carboxymethyl cellulose for curcumin slow-release, *J. Polym. Res.*, 2022, **29**, 487.

42 F. Nemati, M. M. Heravi and R. S. Rad, Nano-Fe_3O_4 encapsulated-silica particles bearing sulfonic acid groups as a magnetically separable catalyst for highly efficient Knoevenagel condensation and Michael addition reactions of aromatic aldehydes with 1, 3-cyclic diketones, *Chin. J. Catal.*, 2012, **33**, 1825–1831.

43 M. Setoodehkhah and S. Momeni, Water Soluble Schiff Base Functinalized Fe_3O_4 Magnetic Nano-Particles as a Novel Adsorbent for the Removal of Pb (II) and Cu (II) Metal Ions from Aqueous Solutions, *J. Inorg. Organomet. Polym. Mater.*, 2018, **28**, 1098–1106.

44 N. D. Cuong, T. T. Hoa, D. Q. Khieu, T. Dai Lam, N. D. Hoa and N. Van Hieu, Synthesis, characterization, and comparative gas-sensing properties of Fe_2O_3 prepared from Fe_3O_4 and Fe_3O_4-chitosan, *J. Alloys Compd.*, 2012, **523**, 120–126.

45 F. Zhang, J. Shi, Y. Jin, Y. Fu, Y. Zhong and W. Zhu, Facile synthesis of MIL-100 (Fe) under HF-free conditions and its application in the acetalization of aldehydes with diols, *Chem. Eng. J.*, 2015, **259**, 183–190.

46 J. Gandara-Loe, I. Ortuño-Lizarán, L. Fernández-Sanchez, J. L. Alió, N. Cuenca, A. Vega-Estrada and J. Silvestre-Albero, Metal–organic frameworks as drug delivery platforms for ocular therapeutics, *ACS Appl. Mater. Interfaces*, 2018, **11**, 1924–1931.

47 Z. Mirzaie, A. Reisi-Vanani and M. Barati, Polyvinyl alcohol-sodium alginate blend, composited with 3D-graphene oxide as a controlled release system for curcumin, *J. Drug Delivery Sci. Technol.*, 2019, **50**, 380–387.

48 Z. Mirzaie, A. Reisi-Vanani, M. Barati and S. M. Atyabi, The drug release kinetics and anticancer activity of the GO/PVA-curcumin nanostructures: The effects of the preparation method and the GO amount, *J.Pharm. Sci.*, 2021, **110**, 3715–3725.

49 S. Dong, S. Ma, Z. L. Liu, L. L. Ma, Y. Zhang, Z. H. Tang, M. X. Deng and W. T. Song, Functional amphiphilic poly (2-oxazoline) block copolymers as drug carriers: the relationship between structure and drug loading capacity, *Chin. J. Polym. Sci.*, 2021, **39**, 865–873.

50 A. Kohan Hoosh Nejad, H. Ahmad Panahi, E. Keshmirizadeh and N. Torabi Fard, Fabrication of a pH-responsive drug delivery system based on the super-paramagnetic metal-organic framework for targeted delivery of oxaliplatin, *Int. J. Polym. Mater. Polym. Biomater.*, 2023, **72**, 1083–1092.

51 R. Nivetha, K. Gothandapani, V. Raghavan, G. Jacob, R. Sellappan, P. Bhardwaj, S. Pitchaimuthu, A. N. M. Kannan, S. K. Jeong and A. N. Grace, Highly porous MIL-100 (Fe) for the hydrogen evolution reaction (HER) in acidic and basic media, *ACS Omega*, 2020, **5**, 18941–18949.

52 Y. Zhao, N. Yuan, D. Bian, J. Sun and G. Qian, Preparation of a novel CSM@ ZIF-67 composite microsphere to facilitate Congo red adsorption from dyeing wastewater, *Environ. Technol.*, 2023, **45**, 2257–2267.

53 M. Afzali, A. Mostafavi and T. Shamspur, A novel electrochemical sensor based on magnetic core@ shell molecularly imprinted nanocomposite (Fe_3O_4@ graphene oxide@ MIP) for sensitive and selective determination of anticancer drug capecitabine, *Arabian J. Chem.*, 2020, **13**, 6626–6638.

54 Z. Sayyar and H. Jafarizadeh Malmiri, Photocatalytic and antibacterial activities study of prepared self-cleaning nanostructure surfaces using synthesized and coated ZnO nanoparticles with Curcumin nanodispersion, *Z. Kristallogr. Cryst. Mater.*, 2019, **234**, 307–328.

55 S. Viturat, M. Thongngam, N. Lumdubwong, W. Zhou and U. Klinkesorn, Ultrasound-assisted formation of chitosan-glucose Maillard reaction products to fabricate nanoparticles with enhanced antioxidant activity, *Ultrason. Sonochem.*, 2023, **97**, 106466.

56 H. Veisi, S. Sajjadifar, P. M. Biabri and S. Hemmati, Oxo-vanadium complex immobilized on chitosan coated-magnetic nanoparticles (Fe_3O_4): A heterogeneous and recyclable nanocatalyst for the chemoselective oxidation of sulfides to sulfoxides with H_2O_2, *Polyhedron*, 2018, **153**, 240–247.

57 J. Joseph, A. Väisänen, A. B. Patil and M. Lahtinen, The effect of synthesis conditions on the *in situ* grown MIL-100 (Fe)-chitosan beads: Interplay between structural properties and arsenic adsorption, *J. Hazard. Mater.*, 2024, **463**, 132893.

58 W. Xie and M. Huang, Enzymatic production of biodiesel using immobilized lipase on core-shell structured Fe3O4@ MIL-100 (Fe) composites, *Catalysts*, 2019, **9**, 850.

59 X. Chen, L. Q. Zou, J. Niu, W. Liu, S. F. Peng and C. M. Liu, The stability, sustained release and cellular antioxidant activity of curcumin nanoliposomes, *Molecules*, 2015, **20**, 14293–14311.

60 P. Z. Hong, S. D. Li, C. Y. Ou, C. P. Li, L. Yang and C. H. Zhang, Thermogravimetric analysis of chitosan, *J. Appl. Polym. Sci.*, 2007, **105**, 547–551.

61 S. Duan, Y. Gao, G. Lan, H. Qiu, B. Xu, Z. Xie, S. Xue and T. Ou, In-situ synthesis of MIL-100 (Fe)@ chitosan composite beads with hierarchical porous structure for efficient adsorption of chlortetracycline hydrochloride: Synthesis, performance and mechanisms, *Sep. Purif. Technol.*, 2024, **333**, 125938.

62 A. Bhattacharjee, M. K. Purkait and S. Gumma, Doxorubicin loading capacity of MIL-100 (Fe): effect of synthesis conditions, *J. Inorg. Organomet. Polym. Mater.*, 2020, **30**, 2366–2375.

63 Z. Chen, Y. Xia, S. Liao, Y. Huang, Y. Li, Y. He, Z. Tong and B. Li, Thermal degradation kinetics study of curcumin with nonlinear methods, *Food Chem.*, 2014, **155**, 81–86.

64 G. Zhao, J. Wang, X. Peng, Y. Li, X. Yuan and Y. Ma, Facile solvothermal synthesis of mesostructured Fe_3O_4/chitosan nanoparticles as delivery vehicles for pH-responsive drug delivery and magnetic resonance imaging contrast agents, *Chem.–Asian J.*, 2014, **9**, 546–553.

65 M. Mohammadikish and S. H. Hashemi, Functionalization of magnetite–chitosan nanocomposite with molybdenum complexes: new efficient catalysts for epoxidation of olefins, *J. Mater. Sci.*, 2019, **54**, 6164–6173.

66 L. Slika and D. Patra, A short review on chemical properties, stability and nano-technological advances for curcumin delivery, *Expert Opin. Drug Delivery*, 2020, **17**, 61–75.
67 W. H. Lee, C. Y. Loo, M. Bebawy, F. Luk, R. S. Mason and R. Rohanizadeh, Curcumin and its derivatives: their application in neuropharmacology and neuroscience in the 21st century, *Curr. neuropharmacol.*, 2013, **14**, 338–378.
68 T. A. Saleh, Kinetic models and thermodynamics of adsorption processes: Classification, in *Interface, science and technology*. vol. 34 (2022) pp. 65–97.
69 B. Obradović, Guidelines for general adsorption kinetics modeling, *Hem. Ind.*, 2020, **74**, 65–70.
70 J. Wang and X. Guo, Adsorption kinetic models: Physical meanings, applications, and solving methods, *J. Hazard. Mater.*, 2020, **390**, 122156.
71 I. Permanadewi, A. C. Kumoro, D. H. Wardhani and N. Aryanti, Modelling of controlled drug release in gastrointestinal tract simulation, *J. Phys.: Conf. Ser.*, 2019, **1295**, 012063.
72 R. Karimi Alavijeh and K. Akhbari, Biocompatible MIL-101 (Fe) as a smart carrier with high loading potential and sustained release of curcumin, *Inorg. Chem.*, 2020, **59**, 3570–3578.
73 P. Sadeh, S. Zeinali, B. Rastegari and I. Najafipour, Functionalization of β-cyclodextrin metal-organic frameworks with gelatin and glutamine for drug delivery of curcumin to cancerous cells, *Heliyon*, 2024, **10**, 1–13.
74 S. Nangare, G. Ramraje and P. Patil, Formulation of lactoferrin decorated dextran based chitosan-coated europium metal-organic framework for targeted delivery of curcumin, *Int. J. Biol. Macromol.*, 2024, **259**, 129325.
75 S. Kazemi, S. Kazemi, M. Pourmadadi, F. Yazdian and A. Ghadami, The synthesis and characterization of targeted delivery curcumin using chitosan-magnetite-reduced graphene oxide as nano-carrier, *Int. J. Biol. Macromol.*, 2021, **186**, 554–562.